ROYAL SOCIETY
OF CHEMISTRY

REVIEW

Check for updates

Surface engineering of anode materials for improving sodium-ion storage performance

Qingbing Xia, [ID] Hanwen Liu and Xiu Song Zhao [ID] *

Sodium-ion batteries (NIBs) are considered a complementary or even an alternative energy storage technology to lithium-ion batteries (LIBs). Current technological development of NIBs is hindered by fundamental challenges, such as sluggish charge transport kinetics, short cycling lifespan, and low energy density. Electrode materials hold the key to any success in commercialising NIBs. While the past decade has witnessed rapid advances in design and synthesis of various electrode materials with different structures and microcosmic morphologies, there are still critical issues associated with electrode materials, especially anode materials, that need to be addressed before the NIB technology becomes commercially viable. For battery electrode materials, their surface properties play a critical role in determining cell performance. As a forefront of an electrode material where Na ion storage and charge transfer initiate, the electrode surface has a fundamental influence on the charge storage properties of the electrode. In this article, we review recent research progress towards modification/ functionalisation of the surface structure of NIB anode materials for improving charge transport kinetics, charge storage capacity, and cycling durability. We aim to provide a concise summary of strategies for surface engineering, along with an insightful analysis of the critical role of the surface structure of NIB anode materials in determining their electrochemical performance.

1. Introduction

With the fast growing market of portable electronic devices, electric vehicles, and grid energy storage, the demand for energy storage devices, like rechargeable batteries, has been drastically increasing. Lithium-ion batteries (LIBs) have profound impact on our daily life because of their high energy and power density coupled with long lifespan.[1–5] However, LIBs are facing severe challenges because lithium resources are geographically unevenly distributed and limited on Earth.[5–8] It is reported that there are only some 14.3 Mt of lithium reserves, of which more than 60% of the accessible lithium resources is in remote or politically sensitive areas.[7,8] Therefore, sustainable battery technologies have been widely explored.[9] Sodium-ion batteries (NIBs) with a similar working principle to that of LIBs have received considerable interest from both academics and industry.[8–11] Sodium is abundant in nature and cost-effective. Thus, NIBs are considered to be a sustainable energy storage technology.[7,10–12] Sodium has a redox potential of −2.71 V *vs.* the standard hydrogen electrode, slightly lower than that of lithium (−3.01 V for lithium *vs.* the standard hydrogen electrode).[10,11,13] The fundamental knowledge on LIBs can be adopted in the NIB chemistry. However, the larger atomic radius of Na^+ (1.02 Å) than Li^+ (0.76 Å) along with the

heavier atomic mass are the disadvantages of NIBs in terms of charge transport kinetics and gravimetric energy density when compared with LIBs.[10–12]

Electrode materials hold the key in determining the battery performance. Cathode materials for NIBs have been extensively investigated over the past decade,[14,15] such as transition-metal layered oxides,[16–18] polyanionic phosphate compounds,[19–21] and Prussian blue phases,[22–24] and some of them can reach a battery performance comparable to that of commercial LIBs with $LiFePO_4$ as the cathode.[8,15] Nevertheless, there are still fundamental challenges such as low coulombic efficiency, severe phase transition, metal ion dissolution, and sluggish charge transport kinetics that need to be solved. On the anode side, carbon,[25–27] metals/alloys,[28–32] and metal oxides/sulphides/ phosphides[13,33–41] are all promising for NIBs. For example, hard carbon materials can deliver a reversible capacity of more than 400 mA h g^{-1} with a Na^+ insertion voltage plateau at about 0.1 V (*vs.* Na^+/Na).[25,42] Sluggish sodiation kinetics is a challenging issue for the anode materials. This mainly originates from their intrinsic low electronic/ionic conductivity and/or multi-step phase change mechanisms during charge/discharge. Besides, large volume change is another crucial issue for many alloying-type and conversion-type anode materials, particularly for phosphorus and transition metal sulphides/phosphides.[43,44] Red phosphorus with a theoretical capacity of ~2600 mA h g^{-1} suffers from a volume expansion of up to ~400% after full sodiation to form Na_3P.[13] Strategies such as using

School of Chemical Engineering, The University of Queensland, St Lucia, QLD 4072, Australia. E-mail: george.zhao@uq.edu.au

This journal is © The Royal Society of Chemistry 2022

J. Mater. Chem. A, 2022, **10**, 3889–3904 | **3889**

nanotechnology to shorten Na ion diffusion pathways,[29,30,33,36] supporting electroactive materials on an electron-conductive support to improve electronic conductivity,[44,45] and heteroatom doping to enhance charge mobility[34,46] are often used to improve electrode performance.

The surface properties of an electrode material play a paramount role in determining the electrode performance. For crystalline materials, their structural symmetry is changed from three-dimensional (3D) in the bulk to two-dimensional (2D) on the surface. Such a discontinuity of the structural order will lead to an energy barrier change for charge transport.[47] Besides, side reactions between the electrode and electrolyte, phase transformation, and volume expansion also bring in changes of structural integrity and chemical/physical properties of the electrode surface, influencing the electrochemical performance. Therefore, the surface properties of electrode materials have significant impacts on charge transport kinetics, charge storage capacity and reversibility, coulombic efficiency, solid electrolyte interphase (SEI), structural integrity, and cycling stability. Recently, surface engineering of electrode materials has become an extremely important solution to improve electrode performance.[34,47–49]

Surface engineering of electrode materials for LIBs,[47,50,51] lithium metal batteries,[52] zinc-ion batteries,[53] or aqueous supercapacitors[54] has been published. However, there is no review on surface engineering of anode materials for NIBs. As illustrated in Fig. 1, the present review summarises recent research progress on strategies for surface modification of NIB anode materials to improve charge transport kinetics, rate capability, charge storage capacity, and cycling stability. Recent review articles on interfacial chemistry in NIBs have been published and are suggested to be read.[55–58]
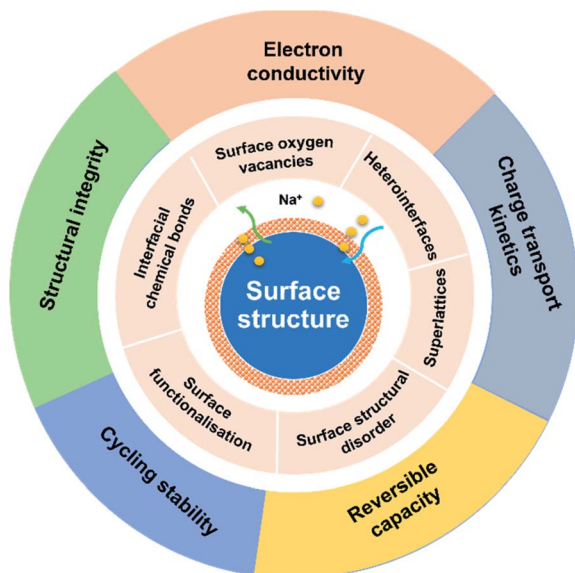

Fig. 1 Illustration of surface structure engineering strategies for improving charge storage capacity, cycling stability, electron and charge conductivity and charge transport kinetics of anode materials for NIBs.

2. Surface oxygen vacancies (OVs)

Metal oxides, such as titanium dioxide (TiO_2),[59–63] tin dioxide (SnO_2),[64,65] vanadium oxide (V_2O_5),[66] and sodium titanate ($Na_2Ti_3O_7$)[67,68] are promising anode candidates for NIBs. For example, TiO_2 has merits of excellent cycling stability and low cost.[69–72] However, the metal oxides suffer from poor rate capability and sluggish sodiation kinetics, originating from their intrinsic semiconducting nature.[34,69,70,73]

Oxygen vacancies (OVs) are present in many metal oxides as point defects. OVs are formed due to the absence of oxygen ions in the crystal lattice as schematically illustrated in Fig. 2a. The presence of OVs changes the local coordination adjacent to them without alternating the intrinsic lattice periodicity, thus altering the local charge distribution and electronic energy levels near the OV site. Introduction of OVs on the surface of metal oxides can significantly enhance electronic conductivity and lower the sodiation energy barrier to facilitate Na ion intercalation and migration kinetics, achieving enhanced charge transport kinetics.[59,74] The typical OV fabrication methods include treatment using a reductant (e.g., $NaHB_4$ or urea)[61,63,67] or in a reductive atmosphere (e.g., H_2),[68] and carbothermal reduction.[65]

Ji and co-workers employed $NaBH_4$ as a reductant to treat anatase to introduce surface OVs into TiO_2.[63] The TiO_2 precursor was ground with $NaHB_4$ in a mass ratio of 2 : 1 to get a uniform mixture, which was heated at 350 °C for 2 h in an Ar atmosphere. Transmission electron microscopy (TEM) images showed a thin layer consisting of OVs and disordered Ti_2O_3 on the surface of modified TiO_2 (Fig. 2b and c). Computational calculations revealed a narrow band gap and reduced energy barriers (5.63 eV in OV-free TiO_2 vs. 4.75 eV in OV-containing TiO_2) for Na ion intercalation in the OV-modified TiO_2, indicating enhancement of electron conductivity. Although enhanced electrochemical performance can be achieved, it's hard to control the OV concentration by using the $NaHB_4$ reductant. Thermal annealing of the TiO_2 nanotubes in a N_2 atmosphere could realize the controllability of OVs by tuning the annealing temperature.[62] It is found that a sample synthesized at 600 °C showed the highest surface OV concentration in the TiO_2 nanotubes and delivered the best Na ion storage performance. The presence of OVs also effectively enhanced the electronic conductivity and reduced the Na ion insertion energy barrier. Kinetic analysis revealed that the Na ion storage proceeded via a pseudocapacitive mechanism, and the charge storage capacity dramatically increased with increasing OV concentration. However, such an OV preparation method involved a high temperature-treatment process, which makes it difficult to apply to the oxide anodes with nanoarchitectures. Gan et al. developed a defect-assisted phosphorus doping strategy to selectively engineer the surface of TiO_2 particles to fabricate a $TiO_2@TiO_{2-x}$–P core@shell architecture.[61] The pinecone-like TiO_2 was first treated by using $NaBH_4$ to generate abundant OVs in the surface region (denoted as $TiO_2@TiO_{2-x}$). Then $TiO@TiO_{2-x}$ was further subjected to a phosphorization process by using NaH_2PO_2 as the P-source at 300 °C, resulting in

3890 | J. Mater. Chem. A, 2022, **10**, 3889–3904
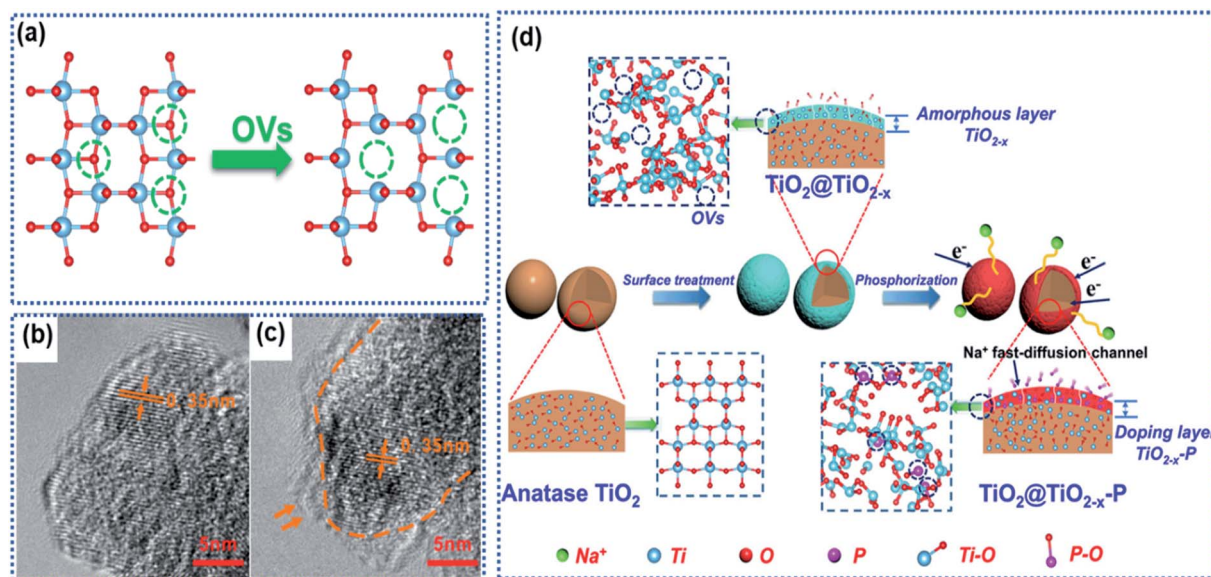
This journal is © The Royal Society of Chemistry 2022

Fig. 2 Surface oxygen vacancies in TiO$_2$: (a) schematic illustration of formation of OVs due to loss of oxygen atoms, (b and c) TEM images of defect-free and defective TiO$_2$ with surface OVs,[63] copyright 2016, American Chemical Society. (d) Schematic illustration of surface OV-induced doping of phosphorus (P).[61] Copyright 2019, American Chemical Society.

the brown-black TiO$_2$@TiO$_{2-x}$–P powder. The core was well crystalline TiO$_2$, while the shell consisted of amorphous TiO$_{2-x}$–P of thickness between 4 and 6 nm and was rich in OVs and Ti^{3+} species (Fig. 2d). The high-resolution TEM (HRTEM) images and the electron paramagnetic resonance (EPR) spectra revealed the existence of OVs, Ti^{3+} species, and the P dopant in the shell, which greatly improved the local electronic conductivity from 4.21×10^{-7} S cm^{-1} (TiO$_2$) to 2.76×10^{-6} S cm^{-1} (TiO$_2$@TiO$_{2-x}$–P) and decreased the Na ion intercalation energy barrier. The oxygen-vacant surface structure acted as a highway for ultrafast electron transport and a buffered zone to efficiently facilitate Na ion interchange between the electrolyte and the bulk of the TiO$_2$ particles, resulting in a promising rate capability with a specific capacity of 167 mA h g^{-1} at 10 A g^{-1} and stable cycling stability with a capacity retention of 98.9% up to 5000 cycles at the same current density. Nevertheless, the synthetic process for TiO$_2$@TiO$_{2-x}$–P involved the utilization of highly toxic phosphine.

Apart from TiO$_2$ anodes, the surface oxygen vacancies have also shown great success in improving the performance of SnO$_2$ anodes. SnO$_2$ with a high theoretical Na ion storage capacity of 1398 mA h g^{-1} holds great promise for NIBs.[73,75] However, the electrochemical performance of SnO$_2$ is greatly hindered by its sluggish sodiation kinetics. The creation of surface OVs has proved to be an effective route to regulate the Na ion intercalation/de-intercalation kinetics of SnO$_2$ anode materials.[64] Ma *et al.* described the preparation of a composite anode material consisting of SnO$_{2-x}$ nanoparticles confined in porous carbon nanofibers (SnO$_{2-x}$/C) by using the electrospinning technique (Fig. 3a).[65] During the high temperature calcination process, the SnO$_2$ crystals were partially reduced to OVs containing-SnO$_{2-x}$ through the carbonthermal reduction (Fig. 3b and c). The experimental results confirmed that the

introduction of OVs effectively enhanced the electronic conductivity of SnO$_{2-x}$ crystals and improved the stability of the interface between discharged products of Sn and Na$_2$O. Besides, the porous carbon nanofibers provided space for buffering the volume changes of the confined SnO$_{2-x}$ nanocrystals. The SnO$_{2-x}$/C composite electrode exhibited a remarkably
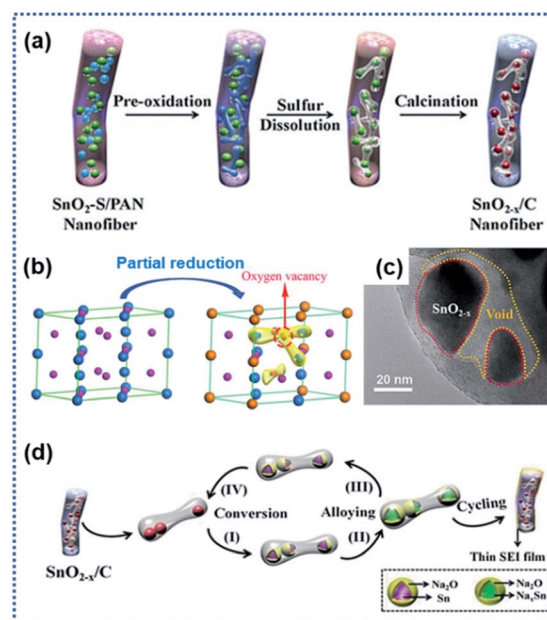

Fig. 3 Surface oxygen vacancies for improving charge transport kinetics of SnO$_2$: (a) schematic illustration of the preparation of SnO$_{2-x}$/C nanofibers, (b) illustration of structural transformation from SnO$_2$ to SnO$_{2-x}$, (c) TEM image of SnO$_{2-x}$/C, and (d) illustration of Na ion intercalation/deintercalation mechanisms in SnO$_{2-x}$/C.[65] Copyright 2018, Wiley-VCH.

enhanced sodiation kinetics and reversibility of conversion reaction Sn ↔ SnO_{2-x} (Fig. 3d). It delivered a discharge capacity of 565 mA h g^{-1} at 1 A g^{-1} after 2000 cycles.

$Na_2Ti_3O_7$ has an average discharging voltage of 0.3 V $vs.$ Na^+/Na and a theoretical Na ion storage capacity of 310 mA h g^{-1}.[70,72,76,77] However, like other metal oxide anode materials, $Na_2Ti_3O_7$ also suffers from sluggish Na insertion/extraction kinetics. Surface OV modulation is a useful approach for facilitating the sodiation kinetics of $Na_2Ti_3O_7$. Fu $et~al.$ synthesized $Na_2Ti_3O_7$ nanoarrays by hydrothermally treating Ti foil in NaOH aqueous solution (Fig. 4a).[68] During the following thermal treatment in an Ar/H_2 atmosphere at 450 °C for 2 h, a crystal structure disordered layer with OVs was formed on the surface of the $Na_2Ti_3O_7$ nanotubes (designated as H–$Na_2Ti_3O_7$, Fig. 4b). The formation of OVs along with Ti^{3+} in the surface layer (Fig. 4c) dramatically enhanced the electrical conductivity from 1.7×10^{-7} S cm^{-1} for air treated $Na_2Ti_3O_7$ (designated as A–$Na_2Ti_3O_7$) to 1.2×10^{-4} S cm^{-1} (H–$Na_2Ti_3O_7$). Meanwhile, the OVs enabled H–$Na_2Ti_3O_7$ to possess a 5-fold higher carrier density than A–$Na_2Ti_3O_7$, drastically reducing the charge transport resistance. H–$Na_2Ti_3O_7$ afforded a high cycling stability of over 10 000 cycles without obvious capacity fading at 35C. Costa $et~al.$ used urea as the reducing agent to form OVs on the surface of $Na_2Ti_3O_7$ particles.[67] At high temperature, urea decomposes into ammonia which further decomposes to produce reactive H_2 that removes oxygen from the $Na_2Ti_3O_7$ structure, forming surface OV decorated $Na_2Ti_3O_7$. It was found that the concentration of OVs could be controlled by controlling the concentration of urea. The introduction of OVs triggered the formation of Ti^{3+} and Ti–OH species, along with a new phase, $Na_2Ti_6O_{13}$ (Fig. 4d). $Ab~initio$ calculations revealed that the presence of OVs leads to electrons from the OVs to be centered on Ti cations and the reduction of Ti^{4+} to Ti^{3+}, resulting in a decrease in the bandgap energy of $Na_2Ti_3O_7$ and an increase in electronic conductivity. The 20 wt% urea sample showed the best electrochemical performance with discharge capacities of 316 mA h g^{-1} at 1C and 272 mA h g^{-1} at 2C. The improved electrochemical performance is attributed to the enhancement of Na ion diffusivity, enhanced charge carrier density, and reduced bandgap energy, which all originate from the surface OVs.

In summary, the surface OV engineering strategy enables one to alter the charge distribution and electronic energy levels of metal oxide anode materials to improve their sodiation kinetics and rate capability. Surface OVs are commonly generated by using the chemical reduction method to remove part of lattice oxygen ions in the metal oxide. Control over the concentration and the distribution uniformity of OVs is a great challenge. Besides, Na ion interaction behavior with the vacancies has not been fully understood. In addition, structural stability of the oxygen-vacant surface during continuous cycling needs to be studied. The core of OVs is used to construct O site defects, and such an anion site engineering conception can be extended to metal sulfides and selenides to construct S or Se vacancies, improving the structural properties.

3. Heterointerfaces

A heterointerface is formed between two dissimilar crystalline materials through lattice-matching, such as between Sb_2S_3 and SnS_2,[78] SnS_2 and SnO_2,[75] Bi_2S_3 and MoS_2,[79] $CoSe_2$ and ZnSe,[80] Fe_2Se_4 and FeSe,[81] Cu_2P_7 and CuP_2,[82] tetragonal SnO_2 and orthorhombic SnO_2,[83] Co_3O_4–CoO,[84] and VO/V_2O_3.[66] The heterointerface between the two crystalline phases can generate a synergistic effect, which is favorable for improving the electrochemical performance of the electrode materials.[79,85–88] At the heterointerface, the Fermi energy difference between the two phases leads to electron transfer across the interface, creating a built-in electric field to induce charge redistribution as schematically illustrated in Fig. 5a. The intrinsic electroneutral phases around the heterointerface are ionized to carry positive charges or negative charges, which can act as active sites for electrochemical reactions and adsorption of opposite charges.[49,89–92]

Fang $et~al.$ developed a Sb_2S_3–SnS_2 hetero-nanostructure using a pulsed-spray evaporation chemical vapor deposition technique to enhance the conversion reaction kinetics (Fig. 5b).[78] DFT calculations showed that the Sb_2S_3 phase had a lower bandgap energy (1.72 eV) than the SnS_2 phase (2.10 eV). The heterointerface resulted in the Fermi energy shifting towards the lower-level potential for the Sb_2S_3 phase and higher-
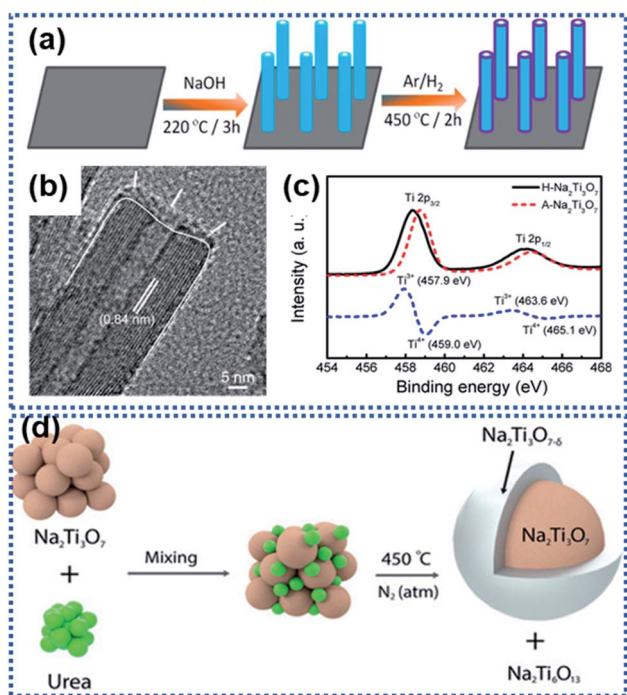

Fig. 4 Examples of creating surface oxygen vacancies in $Na_2Ti_3O_7$: (a) schematic illustration of the preparation of hydrogen-reduced $Na_2Ti_3O_7$ (H–$Na_2Ti_3O_7$), (b) TEM image of H–$Na_2Ti_3O_7$, and (c) Ti 2p XPS spectra of air-treated $Na_2Ti_3O_7$ (A–$Na_2Ti_3O_7$) and H–$Na_2Ti_3O_7$ (the blue dashed line represents the difference between the two XPS spectra).[68] Copyright 2016, American Chemical Society. (d) Schematic illustration of formation of surface OVs on $Na_2Ti_3O_7$ by reaction with urea in a nitrogen atmosphere at 450 °C.[67] Copyright 2021, Wiley-VCH.
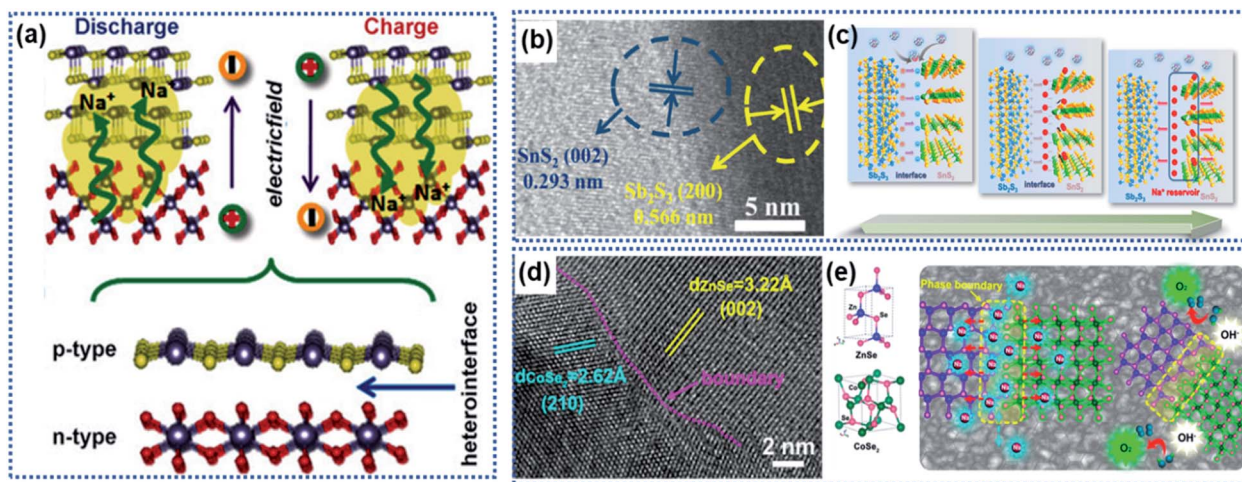
Fig. 5 Heterointerface-induced built-in electric field: (a) schematic illustration of the formation of a built-in electric field due to a hetero-interface.[75] Copyright 2016, Wiley-VCH. (b) High-resolution TEM (HRTEM) image showing the interface formed between Sb_2S_3 and SnS_2. (c) Illustration of the charge storage mechanism induced by the Sb_2S_3–SnS_2 heterointerface.[78] Copyright 2019, Elsevier. (d) HRTEM image and (e) schematic illustration of the CoZn–Se heterointerface.[80] Copyright 2020, American Chemical Society.
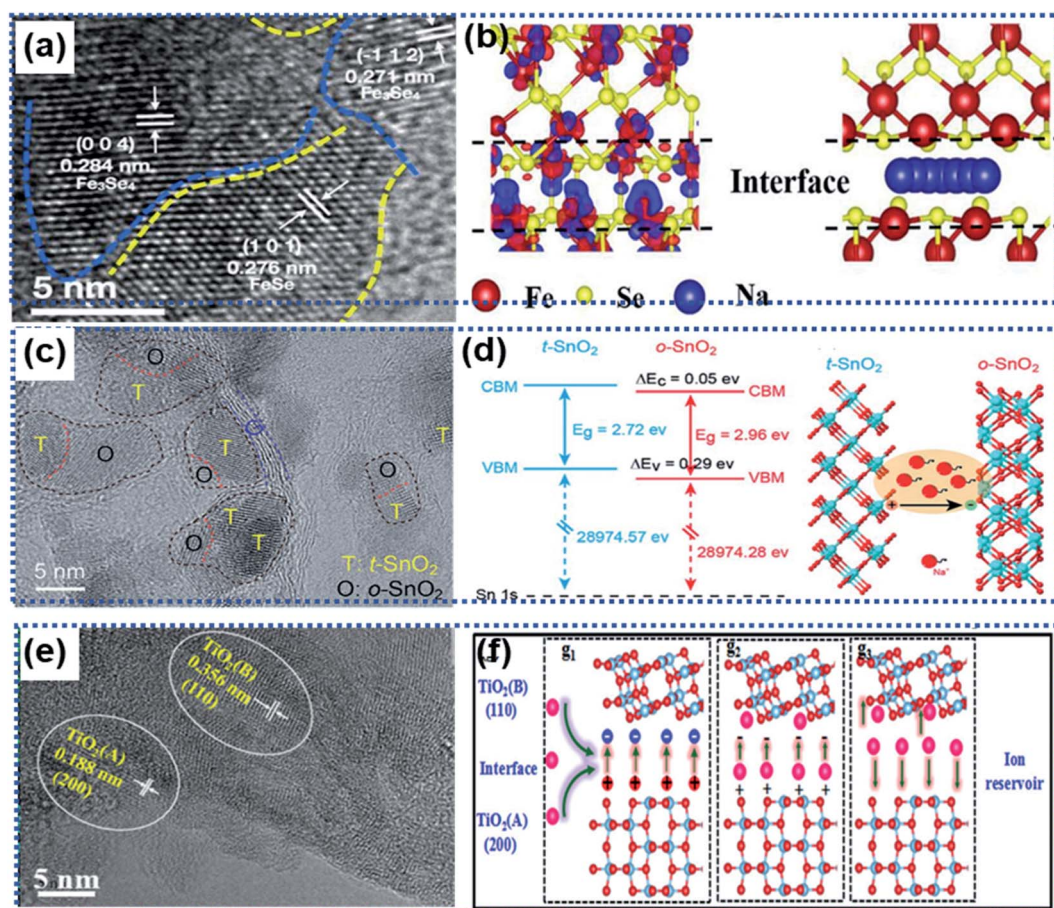

Fig. 6 Roles of heterointerfaces in facilitating efficient charge transport: (a) HRTEM image showing the heterointerface between Fe_3Se_4 and FeSe, (b) schematic illustration of the charge density distribution (left) and Na ion migration pathway (right) along the Fe_3Se_4/FeSe hetero-interface.[81] Copyright 2021, Elsevier. (c) HRTRM image showing the presence of multiple heterointerfaces in a SnO_2/Se/graphene composite. (d) Illustration of band alignments of t-SnO_2 and o-SnO_2 at the heterointerface generating an electric field to accelerate charge transport.[83] Copyright 2018, Royal Society of Chemistry. (e) HRTEM image showing the presence of two TiO_2 phases forming a heterointerface. (f) Schematic illustration of the role of the anatase/TiO_2(B) heterointerface as an ion reservoir for Li^+/Na^+ storage.[87] Copyright 2018, Royal Society of Chemistry.

level potential for the SnS₂ phase, respectively, creating an internal electric field pointing from the Sb₂S₃ phase to the SnS₂ phase. Na ions were strongly attracted to the SnS₂ phase side to reach charge balance until the interfacial electric field disappears. Then, the Na ions migrated to both phases driven by the ion concentration gradient across the heterointerface, achieving a superior conversion reaction kinetics (Fig. 5c). In this work, the Sb₂S₃–SnS₂ heterointerface only achieved 94% capacity retention after 50 cycles. However, both Sb₂S₂ and SnS₂ undergo large volume change upon insertion of Na ions, which may destroy the structural integrity of the Sb₂S₃–SnS₂ heterointerface. Similarly, the heterointerface between CoSe₂ and ZnSe provided a much lower Na ion adsorption energy due to the electron redistribution along the phase boundary (Fig. 5d and e).[80] Theoretical calculations revealed that the band gap difference between the two phases produces a strong electrostatic field across the interface, driving electrons to migrate from the CoSe₂ side to the ZnSe side to accumulate in ZnSe. The electron accumulation leads to strong attraction of Na ions on the phase boundary close to the ZnSe side, thus enabling fast intercalation kinetics.

Local transformation of a primary phase into a secondary phase also leads to the formation of heterointerfaces.[81–84,87] Usually, the two phases are composed of the same elements with a good lattice match. For example, Liu and co-workers reported Fe₃Se₄/FeSe heterointerfaces synthesized via a gas-phase selenisation method (Fig. 6a).[81] The DFT calculation results showed that the Fe₃Se₄/FeSe heterostructure was in a metallic state with a high carrier density near the Fermi level. The charge accumulation occurred not only at the Fe₃Se₄/FeSe heterointerface but also around the Fe atoms to facilitate efficient charge transfer (Fig. 6b), thus enhancing electronic conductivity. Another example is the heterointerface in a Cu₂P₇/CuP₂/C composite material prepared by using the ball milling method, in which carbon was used as a conductive matrix to support the Cu₂P₇/CuP₂ heterostructure.[82] The band gap difference between Cu₂P₇ and CuP₂ enabled the heterointerfaces to not only exhibit more favorable ion/electron transportation but also more electrochemical active sites.

Wang et al. fabricated multiple heterointerfaces, including tetragonal and orthorhombic SnO₂ (t-/o-SnO₂) heterointerfaces and t/o-SnO₂ and the two-phase heterointerfaces between t/o-SnO₂ and a-Se (Fig. 6c), by introducing Se into SnO₂ nanoparticles.[83] The electron flow from the t-SnO₂ phase to the o-SnO₂ phase resulted in multiple built-in electric fields at the heterointerfaces, which significantly boosted the interface sodiation kinetics to realize ultrafast Na ion storage (Fig. 6d). Similarly, the anatase/TiO₂ (B) heterointerface ensured an internal electric field with a high ionic concentration to facilitate the fast charge transport and a low Na ion adsorption energy, giving rise to fast electrochemical kinetics (Fig. 6e and f).[87]

In summary, the unique characteristics of the heterointerface existing in two-phase materials, including built-in electric field, local charge accumulation, and Fermi energy shift, that are not observed in single-phase materials can effectively enhance sodiation reaction kinetics, resulting in a significantly

improved rate capability. The lattice strain around the heterointerface will have a critical impact on the stability of the heterointerface, which needs to be investigated. Alloying-type anode materials, such as SnS₂, Sb₂S₃ and FeSe experience drastic phase changes and large volume expansion during cycling, potentially destroying the stability of the heterointerface. Research work is needed to improve the heterointerface stability.

4. Superlattices

2D superlattices consist of alternately stacked 2D monolayer nanosheets at atomic/molecular levels (Fig. 7a). Monolayer graphene sheets are often used as one of the components to fabricate 2D superlattices for improving electron conductivity.[33,35,46,93–96] The high-quality periodic alternate stacking of the single layers results in an electric charge redistribution at the 2D atomic interface, enhancing charge separation and transfer. Besides, the 2D superlattices can provide an enlarged interlayer distance and enhance the accessibility of active sites to Na ions, leading to a remarkably improved rate capability and charge storage capacity. In addition, the intimate interactions at the 2D interface strengthen the structural stability of the electroactive layers.[97]

Xia and co-workers fabricated highly ordered 2D superlattice nanosheet arrays (SNAs) consisting of titania and carbon sheets with a tunable interlayer spacing between 6.89 and 7.2 Å via a molecularly mediated thermal treatment approach (Fig. 7b).[35] Driven by the thermal treatment, the titania oligomers crystallized to form 2D sheets mediated by the organic molecules, which in reverse catalyzed the organic molecules into carbon layers, forming 2D SNAs. Such 2D SNAs exhibit unique properties, including (1) intimate 2D atomic interface contact between the titania layer and the carbon layer with improved electron conductivity, (2) large interfacial area, providing abundant accessible active sites for Na ions, and (3) increased interlayer spacing, facilitating Na ion diffusion. Furthermore, the authors fabricated a smart sheet-in-shell architecture with the 2D SNAs vertically oriented and encapsulated in hollow carbon spheres decorated with TiO₂ quantum dots, which effectively minimized aggregation of the 2D SNAs. As a result, the 2D SNA architecture presented a nearly zero-strain characteristic during sodiation and a pseudocapacitive-controlled mechanism, achieving an excellent ultrahigh rate capability of up to 50C and superior long-term cycling stability at an ultrahigh rate of 20C over 4000 cycles.

Xiong et al. described a generalised layer-by-layer assemble approach to fabricate 2D superlattices by using single-layer graphene and other electroactive materials (Fig. 8a), including MnO₂,[94] Ti₀.₈₇O₂,[98] and MoS₂,[95] in which the graphene layer not only facilitated electron conduction but also suppressed the volume change of the electroactive materials. For example, MnO₂/graphene consisted of alternately stacked unilamellar MnO₂ nanosheets with graphene monolayers (Fig. 8b and c),[99] in which the unilamellar MnO₂ nanosheets (0.8 nm in thickness) were spatially separated and stabilized between two graphene sheets with a 2.2 nm distance between the adjacent
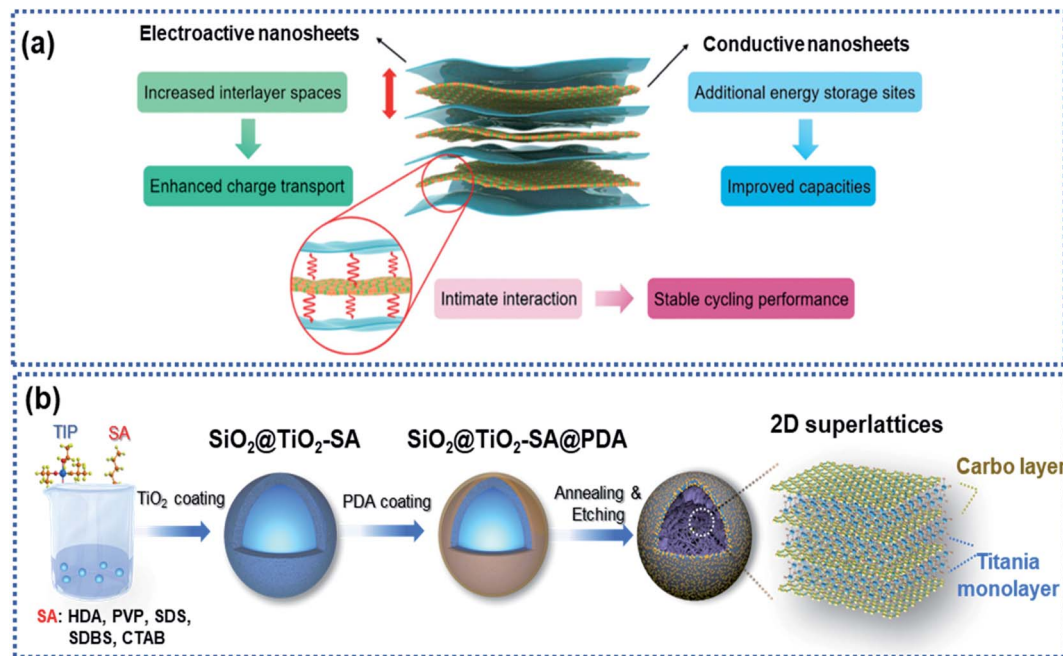
3894 | J. Mater. Chem. A, 2022, **10**, 3889–3904

This journal is © The Royal Society of Chemistry 2022

Fig. 7 Microstructure and fabrication of 2D superlattices: (a) schematic illustration of a 2D superlattice facilitating charge transport and storage.[97] Copyright 2020, Royal Society of Chemistry. (b) Schematic illustration of the fabrication of a 2D superlattice consisting of alternative layers of titania and carbon.[35] Copyright 2019, Wiley-VCH.

MnO_2 nanosheets. The unilamellar MnO_2 nanosheets provided more accessible surface-active sites and shortened Na ion diffusion pathways. Besides, the intimate hybridization between the MnO_2 and graphene nanosheets promoted electron transport throughout the whole superlattice, leading to improved charge transport kinetics. As a result, an excellent rate capability was achieved for both Li and Na storage with capacities of 370 mA h g^{-1} for Li^+ and 245 mA h g^{-1} for Na^+ measured at 12.8 A g^{-1}. Both $Ti_{0.87}O_2$/graphene and MoS_2/graphene superlattices prepared by using this strategy exhibited ultrafast discharge/charge capability.[98] Ti-deficient $Ti_{0.87}O_2$ nanosheets were alternately stacked with nitrogen-doped graphene nanosheets to form a $Ti_{0.87}O_2$/graphene superlattice (Fig. 8d and e), which exhibited ultrahigh rate capability with a specific capacity of ~65 mA h g^{-1} at 51.2 A g^{-1}. The authors also observed a sodium-ion storage capacity of ~100 mA h g^{-1} at 12.8 A g^{-1} measured at −5 °C.[98] DFT calculations revealed that the superlattice can remarkably lower the Na ion diffusion energy barrier from 2.1 eV for $Ti_{0.87}O_2$ to 1.4 eV for the $Ti_{0.87}O_2$/graphene superlattice. The alternative restacking of 1T-MoS_2 single sheets and reduced graphene oxide nanosheets yielded a MoS_2/graphene superlattice (Fig. 8f and g),[95] which delivered specific capacities of 240 mA h g^{-1} at 51.2 A g^{-1} and 380 mA h g^{-1} at 10 A g^{-1} over 1000 cycles due to the dramatically enhanced conductivity in the MoS_2 layers and the widely exposed accessible active sites at the 2D interface.

In summary, 2D superlattices combining the advantages of different 2D components exhibit improved electron conductivity and suppressed volume change of the electroactive component, leading to enhanced rate capability and cycling stability. Presently, the selection of the electroactive components is mainly limited to van der Waals layered materials (like MoS_2), which can be exfoliated from their bulk precursors *via* chemical/physical methods. Superlattices based on non-layered structured materials have been rarely reported. Besides, the layer-by-layer assemble approach to fabricating 2D superlattices is complicated sometimes involving harsh conditions. Rational and scalable approaches deserve investigations for controllable synthesis of high-performance 2D superlattices for Na ion storage.

5. Surface-structural disorder

Structural disorder by breaking the intrinsic atom periodicity arrangement in a crystalline material in a non-repeating variation state as schematically shown in Fig. 9a can dramatically change the charge transport properties inside the material. Structural disorder occurring in the surface region of particles will destroy the periodicity of the lattice spacing while maintaining the bulk integrity, leading to increased accessible active sites for Na ion storage and lowered Na ion migration energy barrier. Usually, the surface structural disorder triggers a pseudocapacitive Na ion storage behavior, which is favorable to realize high electrochemical reaction activity and high-rate capability.[34,60,61,100–104]

Wang *et al.* modified WS_2 nanoparticles *via* hydrogen plasma treatment at 300 °C for 2 h. A disordered layer with a thickness of about 2.5 nm was observed at the surface of the treated WS_2 nanoparticles. This layer was found to significantly lower the charge transport resistance, leading to an enhanced rate capability.[105] Surface phosphorylation on TiO_2 nanotube arrays could boost the Na ion storage (Fig. 9b).[102] The TiO_2 nanotube

This journal is © The Royal Society of Chemistry 2022

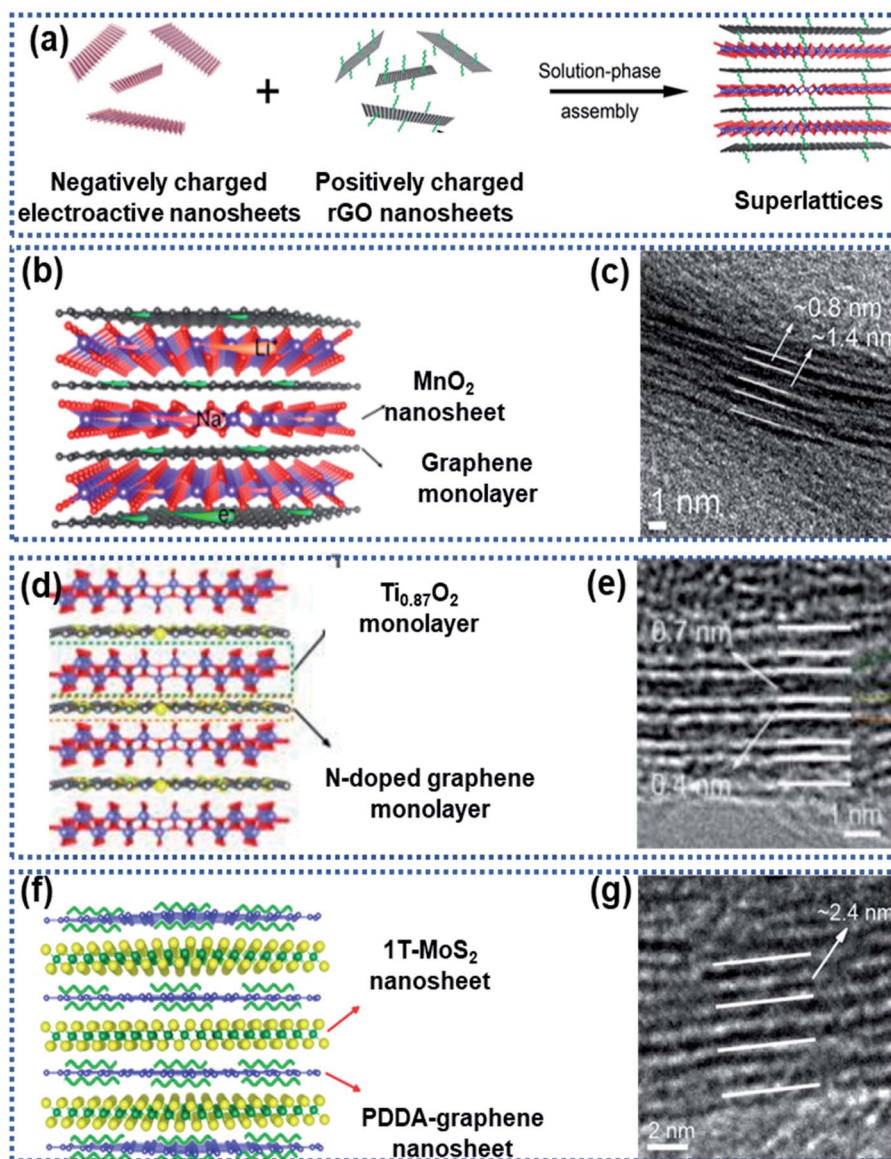*J. Mater. Chem. A*, 2022, **10**, 3889–3904 | **3895**

Fig. 8 Fabrication of 2D superlattices through layer-by-layer assembly: (a) schematic illustration of the layer-by-layer strategy for fabrication of 2D superlattices, (b) structural model and (c) HRTEM image of a MnO_2/graphene superlattice,[94] Copyright 2018, American Chemical Society, (d) structural model and (e) HRTEM image of a $Ti_{0.87}O_2$/graphene superlattice,[98] Copyright 2018, American Chemical Society, and (f) structural model and (g) HRTEM image of a MoS_2/graphene superlattice,[95] Copyright 2018, American Chemical Society.

arrays were annealed in a PH_3 gas environment to yield a disordered phosphorylated TiO_2 layer in the surface region of the nanotubes (P–TiO_2), resulting in surface-structural disorder due to the mismatch between the phosphate and the oxygen groups. Kinetic analysis showed that the P–TiO_2 electrode stored Na ions *via* a pseudocapacitive mechanism, which enables the observed high redox reaction reactivity. As a result, the P–TiO_2 electrode showed a significantly enhanced surface reactivity compared to pure TiO_2 tubes, delivering an initial discharge capacity of 569 mA h g^{-1}, much higher than that of the pure TiO_2 tubes (402 mA h g^{-1}). In addition, the P–TiO_2 anode exhibited an enhanced rate capability with a reversible capacity of 147 mA h g^{-1} at 10C (only 85 mA g^{-1} was achieved by the pure TiO_2) and long-term operating stability with 94% capacity retention after 1000 cycles at 10C.

Although enhanced electrochemical performance owing to surface-structural disorder was observed, rate capability was not obviously improved because of intrinsic sluggish charge transport properties in the bulk electrode material. Xia *et al.* developed a phosphorus modulation strategy to modify the TiO_2 nanocrystals to boost the Na ion storage kinetics of TiO_2 nanocrystals (Fig. 9c).[34] The phosphorization triggered the surface structure disordering while realizing P-doping in the bulk. The electrochemical results showed that the surface-structural disorder enabled a capacitive-controlled Na ion storage behavior with boosted electrochemical activity and reaction kinetics of TiO_2 nanocrystals, achieving an impressive reversible Na ion storage capacity of 210 mA h g^{-1} at 50C. The studies by Ni *et al.*[102] and Xia *et al.*[34] involved PH_3, which is highly toxic and flammable. Plasma treatment and

3896 | *J. Mater. Chem. A*, 2022, **10**, 3889–3904

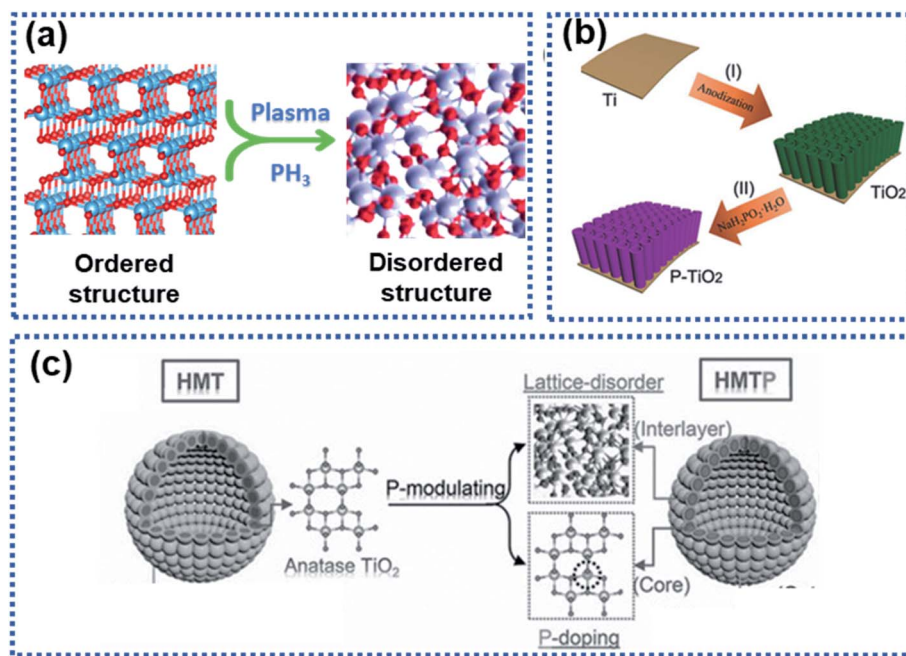This journal is © The Royal Society of Chemistry 2022

Fig. 9 Illustration of surface-structural disorder: (a) schematic illustration of the transition of an ordered crystalline material to become disordered, (b) a scheme showing the synthesis of TiO_2 tubes functionalised with a phosphorylated surface layer,[102] copyright 2018, Wiley-VCH, and (c) schematic illustration of the P-modulation strategy for synthesizing surface-disordered TiO_2.[34] Copyright 2019, Wiley-VCH $Na_2Ti_3O_7$.

hydrogenation are promising approaches to construct a disorder surface layer.[60,89,106]

In summary, surface-structural disorder brings in the surface-controlled pseudocapacitive dominated Na ion storage mechanism, which is favorable for realizing high electrochemical reaction activity and efficient charge transport. Compared with other strategies, the triggered pseudocapacitive-dominated Na ion storage mechanism can significantly improve rate capability. However, this strategy usually does not change the bulk properties (like sluggish Na ion diffusion kinetics, structural instability, lattice expansion upon intercalation of Na ions, *etc.*) of the active materials. The synergistic strategy by combining the surface-structural disorder with the bulk heteroatom doping will be a good way to fully improve the Na ion storage properties of anode materials.

6. Surface functionalisation

Surface functionalisation by introducing electrochemical active sites accessible to Na ions is an effective way to activate the surface electrochemical reactivity. The electrochemical active sites on the surface of anode materials can achieve a rapid electrochemical interaction between the Na ions and the electrode materials, realizing dramatically enhanced surface charge storage properties.[48,107–109] Surface functionalisation strategies, such as introducing functional groups, creating defects, and heteroatom doping are widely used. The active site-dominated electrochemical processes occur in forms of electrocapacitive adsorption and surface redox reactions, which do not involve solid-state ion diffusion in the bulk, thus enabling a fast Na ion storage rate.

Luo and co-workers reported functionalisation of graphene sheets with C=O groups, which are active sites for electrochemical redox reactions with Na ions (Fig. 10a).[110] The C=O-functionalized graphene enabled fast surface adsorption/desorption of Na ions, resulting in significantly improved reaction kinetics compared with graphene without functionalisation. The electrochemical results showed that the C=O-functionalized graphene nanosheets achieved excellent rate capability with a capacity of 214 mA h g^{-1} delivered at 10 A g^{-1} and stable cycling up to 10 000 cycles at 5 A g^{-1} with nearly 100% capacity retention. Sun *et al.* reported that the carboxyl groups on coal derived carbon acted as active sites for surface Na ion capacitive adsorption *via* electrostatic interactions to enhance the Na ion storage performance, including reversible capacity, rate capability, and cycling stability.[111] Commercial carbon black was functionalized by using the thermal treatment method in the presence of CO_2 at 1050 °C (Fig. 10b).[112] The surface of the functionalized carbon black was enriched with carboxyl, carbonyl, and hydroxyl groups, enabling a remarkable pseudocapacitive behavior. In addition, the surface functional groups can significantly facilitate charge transport of Na ions and solvated species, ensuing the rapid capacitive reactions on the defective surface storage, resulting in a reversible capacity of 505 mA h g^{-1} at 50 mA h^{-1}. When the current density was increased to 16 A g^{-1}, the material still delivered a capacity as high as 181 mA h g^{-1} in ether-based electrolytes. Besides, heteroatom doping can also increase surface active sites. Wang *et al.* reported the creation of multiple active-sites in amorphous meso-porous carbon spheres (MAC) *via* N and P element doping (Fig. 10c).[48] It was found that the heteroatom doping creates numerous active sites at the surface of the MAC, facilitating fast and reversible capacitive adsorption of Na ions.
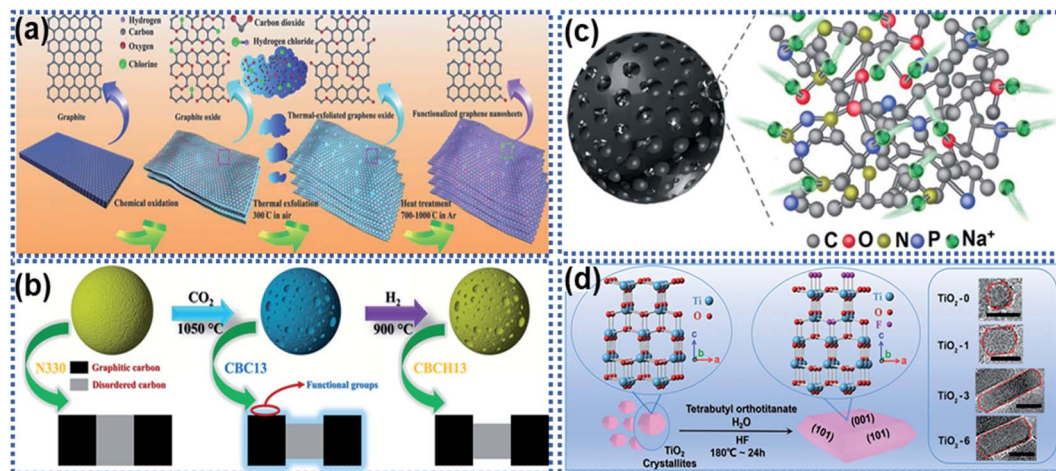
Fig. 10 Schemes illustrating surface functionalisation strategies: (a) schematic illustration of oxygen-functionalized graphene nanosheets,[110] copyright 2018, Wiley-VCH. (b) Illustration of a CO_2 thermal etching route to create surface oxygenated functionalities on a commercial carbon material.[112] Copyright 2020, American Chemical Society. (c) Schematic illustration of multiple active sites on amorphous mesoporous carbon spheres for interacting with Na ions.[48] Copyright 2019, Wiley-VCH. (d) Schematic illustration of a fluorine modulation strategy for regulating the exposed crystal facet in TiO_2 nanocrystals.[113] Copyright 2020, Wiley-VCH.

Apart from introducing functional groups to create surface active sites, surface structure modulation can also enhance the Na ion reaction kinetics with electrode materials. Ni *et al.* proposed a fluorine modulation strategy to functionalize anatase TiO_2 nanocrystals.[113] It was found that the fluorinated TiO_2 ($TiO_{2-x}F_x$) nanocrystals exhibited a high ratio in the (001) facets, which are electrochemically reactive towards Na ions (Fig. 10d). The optimized $TiO_{2-x}F_x$ nanocrystals exhibited a remarkable pseudocapacitive Na ion storage behavior with ultrahigh rate capability. Liu *et al.* reported the surface engineering of $Na_2Ti_3O_7$ nanotube arrays *via* NH_3-assisted calcination.[114] The NH_3-assisted treatment triggered the formation of a highly crystalline surface with self Ti^{3+} doping to achieve favorable Na ion diffusion kinetics and much improved electronic conductivity. The surface activated $Na_2Ti_3O_7$ nanobelts showed improved rate capability with a capacity of 88.5 mA h g^{-1} at 100C and cycling stability with 92.3% capacity retention over 5000 cycles at 50C.

To sum up, surface functionalisation renders anode materials to store Na ions *via* a surface pseudocapacitive redox reaction mechanism, thus enabling significantly improved charge transport kinetics. Compared with other strategies, the surface functionalisation involves facile synthetic methods but show greater success in achieving high-rate capability, partially in carbon-based anode materials. Such a conception can be expanded to hard carbon anodes. Hard carbon anodes show a slop voltage–capacity profile (above 0.1 V) based on the surface Na ion adsorption process. By introduction of carbonyl groups on the surface of hard carbons, more active sites can be created, thus achieving slope-dominated hard carbon with fast discharge/charge capability.

7. Interfacial chemical bonds

High-capacity anode materials such as P, Sn, and alloys suffer from large volume expansion during cycling, leading to the rapid capacity decay. Such materials are often stabilized by using another material to form a composite *via* either physical bonds or chemical bonds or both. The formation of chemical bonds between an electrochemically active material and a support can significantly enhance structural stability of the active component against cycling.[115] The chemical bonds also play an important role in suppressing volume expansion of the electrochemically active material upon sodiation/desodiation. Generally, two types of composite materials have chemical bonds, namely the M–C/S and M–X–C types, where M represents P, Sn, Sb, *etc.*, C stands for carbon, S stands for sulfur, and X represents N, O, *etc.*

For the M–C/S type composite anode materials, covalent bonds are formed between the M and C or S atoms. Li *et al.* employed graphite nanoplates to stabilize red P particles and observed that chemical bonds were formed between P and C. The stability of red P was significantly improved with 92.5% capacity retention after 200 cycles at 1 A g^{-1}.[116] Hu *et al.* reported the hybridization of red P with sulfurized polyacrylonitrile (SPAN) to prepare a composite material with P chemically bonded to SPAN forming composite P–SPAN *via* a mechanical ball-milling process (Fig. 11a).[117] During ball milling, P–S bonds were formed between the P particles and the conductive SPAN matrix to yield P–SPAN, which was shown to be very stable against cycling. The P–SPAN hybrid delivered a specific capacity of 1300 mA h g^{-1} with a capacity retention of 91% after 100 cycles at 520 mA g^{-1}. Sn–C bonds were formed between SnSe and nitrogen-doped carbon (NC) in a composite material (SnSe/NC) synthesized *via* a cation-exchange approach.[118] The chemical Sn–C bonds facilitated electron and ion transport and stabilised the SnSe/NC heterostructure (Fig. 11b), which achieved a good charge storage reversibility with 82% capacity retention after 200 cycles at 2 A g^{-1}.

For the M–X–C type composite materials, the X heteroatom plays an important part in linking the electrochemically active

3898 | *J. Mater. Chem. A*, 2022, **10**, 3889–3904

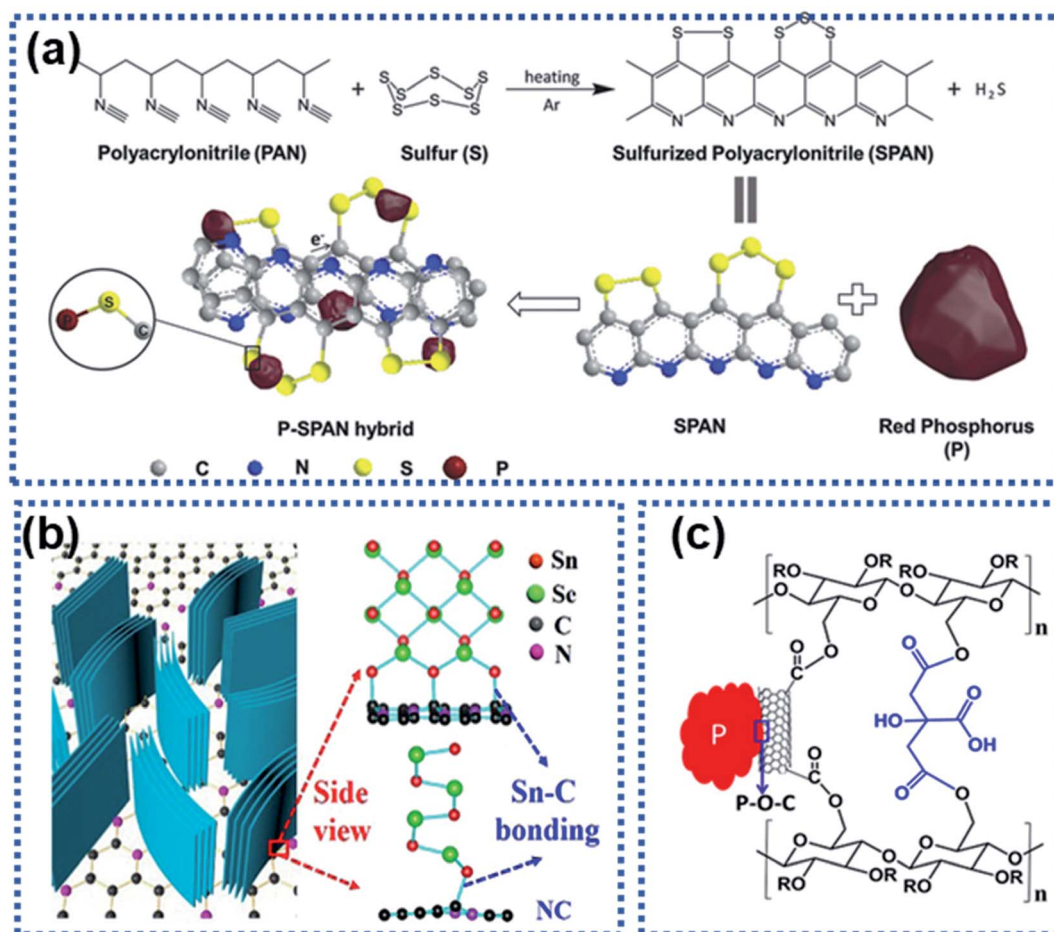This journal is © The Royal Society of Chemistry 2022

Fig. 11 Strategies for constructing the interfacial chemical bond: (a) synthesis of a P–SPAN hybrid material with P–S bonds formed between P and SPAN.[117] Copyright 2018, Wiley-VCH. (b) Schematic illustration of composite SnSe/graphene and the Sn–C bonds formed between SnSe and graphene.[118] Copyright 2018, Elsevier. (c) P–O–C bond interactions between red P and sodium carboxymethyl cellulose–citric acid linked carbon nanotubes.[119] Copyright 2015, American Chemical Society.

material and the support *via* chemical bonding.[115] For instance, Song *et al.* chemically bonded P with multiwalled carbon nanotubes functionalized with carboxylic acid groups through the oxygen atoms (P–CNT, Fig. 11c).[119] The red P particles were chemically bonded to the carbon nanotubes *via* P–O–C bonds, significantly suppressing volume expansion of red P upon sodiation. The P–CNT composite was further bonded with the cross-linked sodium carboxylmethyl cellulose–citric acid binder. The hybrid achieved a specific capacity of 1586.2 mA h g^{-1} over 100 cycles. A similar strategy has been used by Xu *et al.* to synthesize a Sb–carbon hybrid material.[120]

In summary, stabilizing electrochemically active materials on a support *via* chemical bonds can significantly enhance structural integrity, suppress volume expansion, and facilitate electron conductivity between the electroactive material and the support. However, the working mechanism of the interfacial chemical bonds and their coupling interactions lack in-depth understanding. Advanced *in situ*/*operando* characterization techniques in combination with computational simulations/ calculations could be the best approach to revealing the role of the chemical bond between an electrochemical material and

a support in suppressing volume expansion and promoting charge transport across the interface.

8. Comparison of the surface modification strategies

We have discussed surface engineering strategies for improving the electrochemical properties of a range of anode materials for NIBs as summarised in Table 1 and Fig. 12. Surface oxygen vacancies can significantly enhance rate capability. However, the strategy of creating surface oxygen vacancies is applicable to metal oxides with specially designed morphologies only, such as nanotubes,[62] nanoarrays,[68] and nanocrystals.[63,65] Hetero-interfaces and 2D superlattices are promising surface engineering strategies for improving charge transport kinetics by lowering the Na ion diffusion energy barrier. One of the key features of heterointerfaces is the built-in electric field, which results in charge redistribution at the interface, effectively facilitating charge transport and improving rate capability. For alloying- and conversion-type anode materials, it remains challenging to achieve long-term cycling stability due to the

Table 1 Summary of surface engineering strategies for anode materials of NIBs

Strategies	Materials	Electrochemical performance			
		First discharge capacity (mA h g^{-1})/current density (mA g^{-1})	Cycling (mA h g^{-1})/cycling numbers/current density (mA g^{-1}), capacity retention	Rate (m Ah g^{-1})/current density (mA g^{-1})	Ref.
Surface oxygen vacancies (OVs)	Anatase TiO$_2$	206.7/33.6	185.1/500/168, 99.1%	91.2/3360	63
	TiO$_2$ nanotube arrays	220.8/260	140.4/1000/1500, 72.7%		62
	Pinecone-like TiO$_2$	510/50	168/5000/10 000, 99%	167/10 000	61
	SnO$_{2-x}$/carbon nanofibers	634/100	447/2500/2000, 106%	340/5000	65
	Na$_2$Ti$_3$O$_7$ nanoarrays	227/33.4	65/1000/6200	71/6200	68
	Na$_2$Ti$_3$O$_7$ particles	420/17.7	145/100/344	80/1770	67
	Na$_2$Ti$_3$O$_7$ nanofiber arrays	488/177	~160/1000/708, ~92.5%	58/11 328	77
Heterointerfaces	Sb$_2$S$_3$–SnS$_2$	655/500	616/50/500, 94%	510/10 000	78
	CoSe$_2$/ZnSe	416/100	~200/4000/10 000, 84%	263/10 000	80
	SnS/SnO$_2$/graphene	976/30	409/500/810, 73%	430/2430	75
	Bi$_2$S$_3$/MoS$_2$	685/100	323.4/1200/10 000	330.4/5000	79
	Fe$_3$Se$_4$/FeSe@N-doped carbon nanofiber	417.4/500	~300/2000/5000, 89.1%	269.5/10 000	81
	Cu$_2$P$_7$/CuP$_2$/C	1700	1254/100/200, 80%	684/5000	82
	Co$_3$O$_4$–CoO	812.9/25	80.9/50/25	73.3/500	84
2D superlattices	2D titania-carbon superlattice arrays	~750/67	160/4000/6700	130/16 750	35
	Unilamellar MnO$_2$–graphene	~500/100	~500/5000/5000, 90%	245/12 800	94
	Unilamellar Ti$_{0.87}$O$_2$–graphene	490/100	155/10 000/10 000	65/51 200	98
	Unilamellar MoS$_2$–graphene	2220/100	380/1000/10 000	240/51 200	95
Surface-structural disorder	Phosphorus modulated TiO$_2$ nanocrystals	~780/67	190/5000/10 050, 93%	210/16 750	34
	Surface-defect-rich and S doped rutile TiO$_2$	~570/50	128.5/6500/10 000	101.9/10 000	60
	Nitrogen doped TiO$_2$ with a disordered surface layer	621/33.5	61.8/400/335	75/1675	100
	Sulfur-doped TiO$_2$ nanotube arrays	~530/33.5	167/4400/3350, 91%	167/3350	101
	Surface phosphorylated TiO$_2$ nanotube arrays	334/67	141/1000/3350, 94%	147/3350	102
	Na$_2$Ti$_3$O$_7$ nanotube arrays	~530/35.4	78/10 000/1770	84/1770	103
Surface functionalisation	Multiple active site decorated carbon spheres		200/10 000/1000	165/10 000	48
	Amorphous carbon/graphene	230/100	142/2500/500, 83.5%	120/10 000	108
	Carboxyl-dominant oxygen rich carbon	382/30	141/2000/1500, 80.2%	153/2000	111
	Surface oxygenated commercial carbon	505/50	176/1000/3200	181/16 000	112
	Fluorine-modulated TiO$_2$	275/50	~180/6000/2000, 91%	129/10 000	113
Interfacial chemical bond	Red phosphorus/graphene nanoplates	1146/100	649/200/1000, 92.5%	274/10 000	116
	Polymer-sulfurized polyacrylonitrile/phosphorus	~1300/520	1355/100/520, 91%	827/1300	117
	Sn–C bonding riveted SnSe nanoplates	723/25	258/200/2000, 82%	88/20 000	118
	P–O–C bonded red P/CNTs	2100/30	1586.2/100/520, 91.7%	850/5200	119
	Antimony/N-doped carbon	475/100	439/150/100, 94.2%	203/5000	120

mechanical instability of the heterointerface caused by the large volume change upon insertion of Na ions. Strategies of 2D superlattices, surface-structural disorder and surface functionalisation increase surface active sites accessible to Na ions with a reduced sodiation energy barrier, leading to enhanced charge storage capacity. These active sites bring in an electrocapacitance-dominated redox mechanism, enabling fast Na ion storage kinetics. For example, a 2D Ti$_{0.87}$O$_2$/graphene superlattice exhibits an ultra-high rate capability and excellent long-term cycling stability over 10 000 cycles at 10 A g^{-1}.[98] While this surface engineering strategy holds great promise, it is extremely challenging and time-consuming. Plasma treatment and hydrogenation are promising approaches to constructing a disorder surface layer. Surface functionalisation by introducing functional groups, creating defects, and heteroatom doping shows remarkable success in enhancing the rate
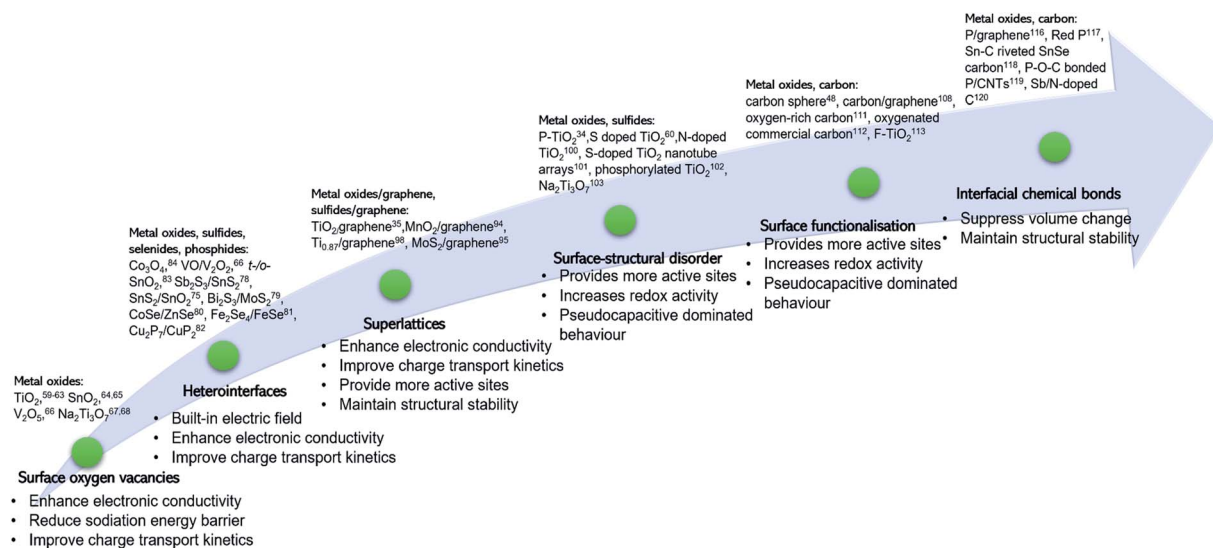
3900 | *J. Mater. Chem. A*, 2022, **10**, 3889–3904

This journal is © The Royal Society of Chemistry 2022

Fig. 12 Summary of how surface modification improves electrode and cell performance of NIBs.

capability of carbonaceous anode materials. Forming chemical bonds, such as P–O–C, P–S, and Sn–C between an active material and a mechanically stable support (*e.g.*, graphene and CNTs) is important to achieve stabilization of the electrode-active material by the support.

9.   Summary and outlook

NIBs are considered as an alternative to LIBs for sustainable, safe and cost-effective energy storage and conversion applications. However, the current NIB technology suffers from sluggish charge transport kinetics, poor cycling stability, and low energy density. Recent advances in surface engineering of anode materials show great promise for boosting the electrochemical performance for sodium ion storage. As the forefront of an electrode material when interacting with Na ions, the surface structural properties of the electrode play a vital role in determining its electrochemical properties.

Over the past decade, significant research progress has been made in improving the electrochemical properties of a wide range of NIB anode materials through surface modification. Further studies are needed for the underlying mechanism of these surface engineering strategies.

Surface oxygen vacancies in metal oxide anodes result in enhanced electronic and ionic conductivity and optimisation of the Na ion migration energy barrier, improving rate capability. Such a strategy can be realised by treating the active materials using reductants or in reducing atmosphere, which shows promise in achieving scalable production. Nevertheless, the oxygen vacancy concentration is usually uncontrollable, and the quantitative control of the oxygen vacancies allows for more precise understanding of the effects of oxygen defects on the electronic structure and the electrochemical properties of anodes. Besides, the structural stability of an oxygen-vacant surface against continuous cycling is hard to predict and lacks in-depth investigation. It is important and interesting to

understand how Na ions interact with oxygen vacancies in metal oxides. In addition, the conception of partially removing anions to construct anion site defects can be extended to metal sulfides and selenides to fabricate S or Se vacancies, improving their electrochemical performance.

Heterointerfaces formed between two crystalline materials with different band gaps through lattice-matching result in a built-in electric field, which can accelerate charge redistribution and facilitate Na ion diffusion, thus improving charge transport kinetics and enhancing rate capability. Nevertheless, for alloying-type anode materials, the severe phase changes and large volume expansion during cycling can destroy the structural integrity of the heterointerface. Therefore, research efforts need to be focused on enhancing the stability of the heterointerfaces to improve Na ion storage properties of anode materials.

2D superlattices assembled from alternately stacked 2D monolayer nanosheets at atomic levels with intimate contacts at the 2D atomic interface possess enriched redox active sites for fast Na ion storage with remarkably enhanced capacity and rate capability. The utilisation of mechanically flexible building blocks, like graphene, can effectively buffer volume expansion and strengthen the structural stability of the active material to achieve long-term cycling durability. However, the existing layer-by-layer synthesis strategy results in low throughput and limited reproducibility. Facile and scalable synthetic approaches need to be developed to realize mass production of high-quality 2D superlattices and to overcome the aggregation issue. Besides, more attention should be paid to understand the Na ion storage mechanism at the 2D atomic interface, which is important in optimising the electrochemical performance.

Surface-structure disorder of anode materials can trigger pseudocapacitance-dominated redox reactions, rendering high capacity and ultrahigh rate capability. However, the widely reported synthetic methods for constructing such a disorder surface layer involve use of highly toxic and flammable PH_3.

This journal is © The Royal Society of Chemistry 2022

J. Mater. Chem. A, 2022, **10**, 3889–3904 | **3901**

Alternative approaches, like plasma treatment and hydrogenation, are more promising and safe.

The formation of chemical bonds is in favor of enhancing the structural stability of the active material against cycling, particularly for anodes of P, Sn, and alloys which suffer from large volume expansion during cycling. However, the working mechanism of the interfacial chemical bonds and their coupling interactions lack in-depth understanding. Advanced *in situ/operando* characterization techniques in combination with computational simulations/calculations could be the best approach to reveal the role of the chemical bond in suppressing volume expansion and understand the charge transfer dynamics across the interface.

All in all, the surface structure engineering will play an increasingly important role in electrode optimization to push the sodium-ion technology to become a reality in this beyond-lithium era.

Conflicts of interest

There are no conflicts to declare.

Acknowledgements

References

1 B. Dunn, H. Kamath and J. M. Tarascon, *Science*, 2011, **334**, 928–935.

2 D. Larcher and J. M. Tarascon, *Nat. Chem.*, 2015, **7**, 19–29.

3 Z. Yang, J. Zhang, M. C. W. Kintner-Meyer, X. Lu, D. Choi, J. P. Lemmon and J. Liu, *Chem. Rev.*, 2011, **111**, 3577–3613.

4 D. M. Davies, M. G. Verde, O. Mnyshenko, Y. R. Chen, R. Rajeev, Y. S. Meng and G. Elliott, *Nat. Energy*, 2018, **4**, 42–50.

5 M. Palacín and A. de Guibert, *Science*, 2016, **351**, 1253292.

6 J.-M. Tarascon, *Nat. Chem.*, 2010, **2**, 510.

7 C. Vaalma, D. Buchholz, M. Weil and S. Passerini, *Nat. Rev. Mater.*, 2018, **3**, 18013.

8 R. Usiskin, Y. X. Lu, J. Popovic, M. Law, P. Balaya, Y. S. Hu and J. Maier, *Nat. Rev. Mater.*, 2021, **6**, 1020–1035.

9 J.-M. Tarascon, *Joule*, 2020, **4**, 1616–1620.

10 N. Yabuuchi, K. Kubota, M. Dahbi and S. Komaba, *Chem. Rev.*, 2014, **114**, 11636–11682.

11 J. Y. Hwang, S. T. Myung and Y. K. Sun, *Chem. Soc. Rev.*, 2017, **46**, 3529–3614.

12 T. Liu, Y. Zhang, Z. Jiang, X. Zeng, J. Ji, Z. Li, X. Gao, M. Sun, Z. Lin, M. Ling, J. Zheng and C. Liang, *Energy Environ. Sci.*, 2019, **12**, 1512–1533.

13 Q. B. Xia, W. J. Li, Z. C. Miao, S. L. Chou and H. K. Liu, *Nano Res.*, 2017, **10**, 4055–4081.

14 L. Li, Y. Zheng, S. Zhang, J. Yang, Z. Shao and Z. Guo, *Energy Environ. Sci.*, 2018, **11**, 2310–2340.

15 X. Xiang, K. Zhang and J. Chen, *Adv. Mater.*, 2015, **27**, 5343–5364.

16 Y. Yang, Y. Feng, Z. Chen, Y. Feng, Q. Huang, C. Ma, Q. Xia, C. Liang, L. Zhou, M. S. Islam, P. Wang, L. Zhou, L. Mai and W. Wei, *Nano Energy*, 2020, **76**, 105061.

17 C. Zhao, Q. Wang, Z. Yao, J. Wang, B. Sánchez-Lengeling, F. Ding, X. Qi, Y. Lu, X. Bai, B. Li, H. Li, A. Aspuru-Guzik, X. Huang, C. Delmas, M. Wagemaker, L. Chen and Y.-S. Hu, *Science*, 2020, **370**, 708.

18 C. Wang, L. Liu, S. Zhao, Y. Liu, Y. Yang, H. Yu, S. Lee, G.-H. Lee, Y.-M. Kang, R. Liu, F. Li and J. Chen, *Nat. Commun.*, 2021, **12**, 2256.

19 J. Zhang, C. Lin, Q. Xia, C. Wang and X. S. Zhao, *ACS Energy Lett.*, 2021, **6**, 2081–2089.

20 X. Shen, Q. Zhou, M. Han, X. Qi, B. Li, Q. Zhang, J. Zhao, C. Yang, H. Liu and Y.-S. Hu, *Nat. Commun.*, 2021, **12**, 2848.

21 J. Zhang, Y. Liu, X. Zhao, L. He, H. Liu, Y. Song, S. Sun, Q. Li, X. Xing and J. Chen, *Adv. Mater.*, 2020, **32**, 1906348.

22 W. Li, C. Han, W. Wang, Q. Xia, S. Chou, Q. Gu, B. Johannessen, H. Liu and S. Dou, *Adv. Energy Mater.*, 2020, **10**, 1903006.

23 W. Li, C. Han, Q. Xia, K. Zhang, S. Chou, Y.-M. Kang, J. Wang, H. K. Liu and S. X. Dou, *Small Methods*, 2018, **2**, 1700346.

24 W. Wang, Y. Gang, Z. Hu, Z. Yan, W. Li, Y. Li, Q.-F. Gu, Z. Wang, S.-L. Chou, H.-K. Liu and S.-X. Dou, *Nat. Commun.*, 2020, **11**, 980.

25 D. Chen, W. Zhang, K. Luo, Y. Song, Y. Zhong, Y. Liu, G. Wang, B. Zhong, Z. Wu and X. Guo, *Energy Environ. Sci.*, 2021, **14**, 2244–2262.

26 A. P. Cohn, K. Share, R. Carter, L. Oakes and C. L. Pint, *Nano Lett.*, 2016, **16**, 543–548.

27 H. S. Hou, X. Q. Qiu, W. F. Wei, Y. Zhang and X. B. Ji, *Adv. Energy Mater.*, 2017, **7**, 1602898.

28 L. Wang, J. Światowska, S. Dai, M. Cao, Z. Zhong, Y. Shen and M. Wang, *Materials Today Energy*, 2019, **11**, 46–60.

29 J. Liu, L. Yu, C. Wu, Y. Wen, K. Yin, F. K. Chiang, R. Hu, J. Liu, L. Sun, L. Gu, J. Maier, Y. Yu and M. Zhu, *Nano Lett.*, 2017, **17**, 2034–2042.

30 J. Zhou, J. Chen, M. Chen, J. Wang, X. Liu, B. Wei, Z. Wang, J. Li, L. Gu, Q. Zhang, H. Wang and L. Guo, *Adv. Mater.*, 2019, **31**, 1807874.

31 M. Mao, F. Yan, C. Cui, J. Ma, M. Zhang, T. Wang and C. Wang, *Nano Lett.*, 2017, **17**, 3830–3836.

32 J. Liu, Z. Yang, J. Wang, L. Gu, J. Maier and Y. Yu, *Nano Energy*, 2015, **16**, 389–398.

33 Q. B. Xia, Y. R. Liang, Z. H. Lin, S. W. Wang, W. H. Lai, D. Yuan, Y. H. Dou, Q. F. Gu, J. Z. Wang, H. K. Liu, S. X. Dou, S. M. Fang and S. L. Chou, *Adv. Energy Mater.*, 2020, **10**, 2001033.

34 Q. Xia, Y. Huang, J. Xiao, L. Wang, Z. Lin, W. Li, H. Liu, Q. Gu, H. K. Liu and S. L. Chou, *Angew. Chem. Int. Ed.*, 2019, **58**, 4022–4026.

35 Q. Xia, Z. Lin, W. Lai, Y. Wang, C. Ma, Z. Yan, Q. Gu, W. Wei, J. Z. Wang, Z. Zhang, H. K. Liu, S. X. Dou and S. L. Chou, *Angew. Chem., Int. Ed.*, 2019, **58**, 14125–14128.

3902 | *J. Mater. Chem. A*, 2022, **10**, 3889–3904

This journal is © The Royal Society of Chemistry 2022

36 J. Ru, T. He, B. Chen, Y. Feng, L. Zu, Z. Wang, Q. Zhang, T. Hao, R. Meng, R. Che, C. Zhang and J. Yang, *Angew. Chem., Int. Ed.*, 2020, **59**, 14621–14627.

37 X. Xu, R. Zhao, B. Chen, L. Wu, C. Zou, W. Ai, H. Zhang, W. Huang and T. Yu, *Adv. Mater.*, 2019, **31**, e1900526.

38 L. Wang, X. Bi and S. Yang, *Adv. Mater.*, 2016, **28**, 7672–7679.

39 D. Zhao, R. Zhao, S. Dong, X. Miao, Z. Zhang, C. Wang and L. Yin, *Energy Environ. Sci.*, 2019, **12**, 2422–2432.

40 X. Wang, Y. Chen, Y. Fang, J. Zhang, S. Gao and X. W. D. Lou, *Angew. Chem., Int. Ed.*, 2019, **58**, 2675–2679.

41 Z. M. Liu, T. C. Lu, T. Song, X. Y. Yu, X. W. Lou and U. Paik, *Energy Environ. Sci.*, 2017, **10**, 1576–1580.

42 M. Thompson, Q. Xia, Z. Hu and X. S. Zhao, *Mater. Adv.*, 2021, **2**, 5881–5905.

43 Z. Hu, L. Wang, K. Zhang, J. Wang, F. Cheng, Z. Tao and J. Chen, *Angew. Chem., Int. Ed.*, 2014, **53**, 12794–12798.

44 J. Sun, H. W. Lee, M. Pasta, H. T. Yuan, G. Y. Zheng, Y. M. Sun, Y. Z. Li and Y. Cui, *Nat. Nanotechnol.*, 2015, **10**, 980–U184.

45 P. Xiong, P. Bai, A. Li, B. Li, M. Cheng, Y. Chen, S. Huang, Q. Jiang, X. H. Bu and Y. Xu, *Adv. Mater.*, 2019, **31**, e1904771.

46 Y. Tian, J. Julio Gutiérrez Moreno, Z. Lu, L. Li, M. Hu, D. Liu, Z. Jian and X. Cai, *Chem. Eng. J.*, 2021, **407**, 127198.

47 L. Yang, K. Yang, J. Zheng, K. Xu, K. Amine and F. Pan, *Chem. Soc. Rev.*, 2020, **49**, 4667–4680.

48 G. Wang, M. Shao, H. Ding, Y. Qi, J. Lian, S. Li, J. Qiu, H. Li and F. Huo, *Angew. Chem., Int. Ed.*, 2019, **58**, 13584–13589.

49 T. Zhou, Y. Zheng, H. Gao, S. Min, S. Li, H. K. Liu and Z. Guo, *Adv. Sci.*, 2015, **2**, 1500027.

50 K. Share, A. Westover, M. Li and C. L. Pint, *Chem. Eng. Sci.*, 2016, **154**, 3–19.

51 W. Luo, X. Chen, Y. Xia, M. Chen, L. Wang, Q. Wang, W. Li and J. Yang, *Adv. Energy Mater.*, 2017, **7**, 1701083.

52 L. Wang, Z. Zhou, X. Yan, F. Hou, L. Wen, W. Luo, J. Liang and S. X. Dou, *Energy Storage Materials*, 2018, **14**, 22–48.

53 B. Li, X. Zhang, T. Wang, Z. He, B. Lu, S. Liang and J. Zhou, *Nano-Micro Letters*, 2021, **14**, 6.

54 C. Xu, H. Yang, J. Li, J. Wang and X. Lu, *Chemelectrochem*, 2020, **7**, 586–593.

55 Y. Huang, L. Zhao, L. Li, M. Xie, F. Wu and R. Chen, *Adv. Mater.*, 2019, **31**, e1808393.

56 H. Y. Che, S. L. Chen, Y. Y. Xie, H. Wang, K. Amine, X. Z. Liao and Z. F. Ma, *Energy Environ. Sci.*, 2017, **10**, 1075–1101.

57 W. Liu, P. Liu and D. Mitlin, *Adv. Energy Mater.*, 2020, **10**, 2002297.

58 Y. Sun, P. Shi, H. Xiang, X. Liang and Y. Yu, *Small*, 2019, **15**, 1805479.

59 Q. Wang, S. Zhang, H. He, C. Xie, Y. Tang, C. He, M. Shao and H. Wang, *Chem. - Asian J.*, 2021, **16**, 3–19.

60 H. He, D. Huang, W. Pang, D. Sun, Q. Wang, Y. Tang, X. Ji, Z. Guo and H. Wang, *Adv. Mater.*, 2018, **30**, e1801013.

61 Q. Gan, H. He, Y. Zhu, Z. Wang, N. Qin, S. Gu, Z. Li, W. Luo and Z. Lu, *ACS Nano*, 2019, **13**, 9247–9258.

62 J. Chen, Y. Fu, F. Sun, Z. Hu, X. Wang, T. Zhang, F. Zhang, X. Wu, H. Chen, G. Cheng and R. Zheng, *Chem. Eng. J.*, 2020, **400**, 125784.

63 J. Chen, Z. Ding, C. Wang, H. Hou, Y. Zhang, C. Wang, G. Zou and X. Ji, *ACS Appl. Mater. Interfaces*, 2016, **8**, 9142–9151.

64 D. Ma, Y. Li, P. Zhang and Z. Lin, *ChemSusChem*, 2018, **11**, 3693–3703.

65 D. Ma, Y. Li, H. Mi, S. Luo, P. Zhang, Z. Lin, J. Li and H. Zhang, *Angew. Chem., Int. Ed.*, 2018, **57**, 8901–8905.

66 Q. Ren, N. Qin, B. Liu, Y. Yao, X. Zhao, Z. Deng, Y. Li, Y. Dong, D. Qian, B.-L. Su, W. Zhang and H.-E. Wang, *J. Mater. Chem. A*, 2020, **8**, 3450–3458.

67 S. I. R. Costa, Y.-S. Choi, A. J. Fielding, A. J. Naylor, J. M. Griffin, Z. Sofer, D. O. Scanlon and N. Tapia-Ruiz, *Chem. - Eur. J.*, 2021, **27**, 3875–3886.

68 S. Fu, J. Ni, Y. Xu, Q. Zhang and L. Li, *Nano Lett.*, 2016, **16**, 4544–4551.

69 C. Chen, Y. Wen, X. Hu, X. Ji, M. Yan, L. Mai, P. Hu, B. Shan and Y. Huang, *Nat. Commun.*, 2015, **6**, 6929.

70 N. N. Wang, C. X. Chu, X. Xu, Y. Du, J. Yang, Z. C. Bai and S. X. Dou, *Adv. Energy Mater.*, 2018, **8**, 1801888.

71 S. H. Guo, J. Yi, Y. Sun and H. S. Zhou, *Energy Environ. Sci.*, 2016, **9**, 2978–3006.

72 S. Lou, Y. Zhao, J. Wang, G. Yin, C. Du and X. Sun, *Small*, 2019, **15**, 1904740.

73 Z. Li, J. Ding and D. Mitlin, *Acc. Chem. Res.*, 2015, **48**, 1657–1665.

74 Z. Su, J. Liu, M. Li, Y. Zhu, S. Qian, M. Weng, J. Zheng, Y. Zhong, F. Pan and S. Zhang, *Electrochem. Energy Rev.*, 2020, **3**, 286–343.

75 Y. Zheng, T. Zhou, C. Zhang, J. Mao, H. Liu and Z. Guo, *Angew. Chem., Int. Ed.*, 2016, **55**, 3408–3413.

76 N. Wang, X. Xu, T. Liao, Y. Du, Z. Bai and S. Dou, *Adv. Mater.*, 2018, **30**, e1804157.

77 D. Kong, Y. Wang, S. Huang, Y. V. Lim, J. Zhang, L. Sun, B. Liu, T. Chen, P. Valdivia y Alvarado and H. Y. Yang, *J. Mater. Chem. A*, 2019, **7**, 12751–12762.

78 L. Fang, Z. Lan, W. Guan, P. Zhou, N. Bahlawane, W. Sun, Y. Lu, C. Liang, M. Yan and Y. Jiang, *Energy Storage Materials*, 2019, **18**, 107–113.

79 L. Cao, X. Liang, X. Ou, X. Yang, Y. Li, C. Yang, Z. Lin and M. Liu, *Adv. Funct. Mater.*, 2020, **30**, 1910732.

80 G. Fang, Q. Wang, J. Zhou, Y. Lei, Z. Chen, Z. Wang, A. Pan and S. Liang, *ACS Nano*, 2019, **13**, 5635–5645.

81 J. Liu, S. Xiao, X. Li, Z. Li, X. Li, W. Zhang, Y. Xiang, X. Niu and J. S. Chen, *Chem. Eng. J.*, 2021, **417**, 129279.

82 X. W. Li, J. Liao, P. F. Shen, X. Lia, Y. Y. Li, N. Li, Z. H. Li, Z. C. Shi, H. Y. Zhang and W. W. Li, *J. Alloys Compd.*, 2019, **803**, 804–811.

83 Y.-Y. Wang, B.-H. Hou, Y.-N. Wang, H.-Y. Lü, J.-Z. Guo, Q.-L. Ning, J.-P. Zhang, C.-L. Lü and X.-L. Wu, *J. Mater. Chem. A*, 2018, **6**, 6578–6586.

84 Y. Liu, H. Wan, H. Zhang, J. Chen, F. Fang, N. Jiang, W. Zhang, F. Zhou, H. Arandiyan, Y. Wang, G. Liu, Z. Wang, S. Luo, X. Chen and H. Sun, *ACS Appl. Nano Mater.*, 2020, **3**, 3892–3903.

This journal is © The Royal Society of Chemistry 2022

J. Mater. Chem. A, 2022, **10**, 3889–3904 | **3903**

85 Y. Li, J. Zhang, Q. Chen, X. Xia and M. Chen, *Adv. Mater.*, 2021, **33**, 2100855.

86 S. Chen, S. Huang, J. Hu, S. Fan, Y. Shang, M. E. Pam, X. Li, Y. Wang, T. Xu, Y. Shi and H. Y. Yang, *Nano-Micro Letters*, 2019, **11**, 80.

87 G. Liu, H.-H. Wu, Q. Meng, T. Zhang, D. Sun, X. Jin, D. Guo, N. Wu, X. Liu and J.-K. Kim, *Nanoscale Horiz.*, 2020, **5**, 150–162.

88 B. Zhao, Q. Q. Liu, Y. J. Chen, Q. Liu, Q. Yu and H. B. Wu, *Adv. Funct. Mater.*, 2020, **30**, 2002019.

89 T. Xia, W. Zhang, J. Murowchick, G. Liu and X. Chen, *Nano Lett.*, 2013, **13**, 5289–5296.

90 W. Luo, F. Li, Q. Li, X. Wang, W. Yang, L. Zhou and L. Mai, *ACS Appl. Mater. Interfaces*, 2018, **10**, 7201–7207.

91 J. Ni, M. Sun and L. Li, *Adv. Mater.*, 2019, **31**, 1902603.

92 W. Li, Q. Song, M. Li, Y. Yuan, J. Zhang, N. Wang, Z. Yang, J. Huang, J. Lu and X. Li, *Small Methods*, 2021, **5**, 2100444.

93 P. Xiong, B. Sun, N. Sakai, R. Ma, T. Sasaki, S. Wang, J. Zhang and G. Wang, *Adv. Mater.*, 2019, e1902654.

94 P. Xiong, R. Ma, N. Sakai and T. Sasaki, *ACS Nano*, 2018, **12**, 1768–1777.

95 P. Xiong, R. Ma, N. Sakai, L. Nurdiwijayanto and T. Sasaki, *ACS Energy Lett.*, 2018, **3**, 997–1005.

96 E. Pomerantseva and Y. Gogotsi, *Nat. Energy*, 2017, **2**, 17089.

97 P. Xiong, Y. Wu, Y. Liu, R. Ma, T. Sasaki, X. Wang and J. Zhu, *Energy Environ. Sci.*, 2020, **13**, 4834–4853.

98 P. Xiong, X. Zhang, F. Zhang, D. Yi, J. Zhang, B. Sun, H. Tian, D. Shanmukaraj, T. Rojo, M. Armand, R. Ma, T. Sasaki and G. Wang, *ACS Nano*, 2018, **12**, 12337–12346.

99 Y. Jiang, M. Sun, J. Ni and L. Li, *ACS Appl. Mater. Interfaces*, 2019, **11**, 37761–37767.

100 H. Wang, J. Xiong, X. Cheng, G. Chen, T. Kups, D. Wang and P. Schaaf, *Sustainable Energy Fuels*, 2019, **3**, 2688–2696.

101 J. Ni, S. Fu, C. Wu, J. Maier, Y. Yu and L. Li, *Adv. Mater.*, 2016, **28**, 2259–2265.

102 J. Ni, S. Fu, Y. Yuan, L. Ma, Y. Jiang, L. Li and J. Lu, *Adv. Mater.*, 2018, **30**, 1704337.

103 J. F. Ni, S. D. Fu, C. Wu, Y. Zhao, J. Maier, Y. Yu and L. Li, *Adv. Energy Mater.*, 2016, **6**, 1502568.

104 S. Yan, K. P. Abhilash, L. Tang, M. Yang, Y. Ma, Q. Xia, Q. Guo and H. Xia, *Small*, 2019, **15**, 1804371.

105 H. Wang, Q. Yuan, D. Wang, G. Chen, X. Cheng, T. Kups and P. Schaaf, *Sustainable Energy Fuels*, 2019, **3**, 865–874.

106 T. Xia, W. Zhang, W. Li, N. A. Oyler, G. Liu and X. Chen, *Nano Energy*, 2013, **2**, 826–835.

107 Y. Zhang, Y. Huang, V. Srot, P. A. van Aken, J. Maier and Y. Yu, *Nano-Micro Letters*, 2020, **12**, 165.

108 S. Li, J. Qiu, C. Lai, M. Ling, H. Zhao and S. Zhang, *Nano Energy*, 2015, **12**, 224–230.

109 B. Babu, P. Simon and A. Balducci, *Adv. Energy Mater.*, 2020, **10**, 2001128.

110 D. Luo, J. Xu, Q. Guo, L. Fang, X. Zhu, Q. Xia and H. Xia, *Adv. Funct. Mater.*, 2018, **28**, 1805371.

111 F. Sun, H. Wang, Z. Qu, K. Wang, L. Wang, J. Gao, J. Gao, S. Liu and Y. Lu, *Adv. Energy Mater.*, 2021, **11**, 2002981.

112 W. Xiao, Q. Sun, J. Liu, B. Xiao, X. Li, P.-A. Glans, J. Li, R. Li, X. Li, J. Guo, W. Yang, T.-K. Sham and X. Sun, *ACS Appl. Mater. Interfaces*, 2020, **12**, 37116–37127.

113 M. Ni, D. Sun, X. Zhu, Q. Xia, Y. Zhao, L. Xue, J. Wu, C. Qiu, Q. Guo, Z. Shi, X. Liu, G. Wang and H. Xia, *Small*, 2020, **16**, 2006366.

114 J. Liu, Z. Wang, Z. Lu, L. Zhang, F. Xie, A. Vasileff and S.-Z. Qiao, *ACS Mater. Lett.*, 2019, **1**, 389–398.

115 S. Li, L. Zhang, W. Zhao, S. Yuan, L. Yang, X. Chen, P. Ge, W. Sun and X. Ji, *Energy Storage Materials*, 2020, **32**, 477–496.

116 W.-J. Li, S.-L. Chou, J.-Z. Wang, H.-K. Liu and S.-X. Dou, *J. Mater. Chem. A*, 2016, **4**, 505–511.

117 Y. Hu, B. Li, X. Jiao, C. Zhang, X. Dai and J. Song, *Adv. Funct. Mater.*, 2018, **28**, 1801010.

118 X. Ren, J. Wang, D. Zhu, Q. Li, W. Tian, L. Wang, J. Zhang, L. Miao, P. K. Chu and K. Huo, *Nano Energy*, 2018, **54**, 322–330.

119 J. Song, Z. Yu, M. L. Gordin, X. Li, H. Peng and D. Wang, *ACS Nano*, 2015, **9**, 11933–11941.

120 X. Xu, L. Si, X. Zhou, F. Tu, X. Zhu and J. Bao, *J. Power Sources*, 2017, **349**, 37–44.

3904 | *J. Mater. Chem. A*, 2022, **10**, 3889–3904

This journal is © The Royal Society of Chemistry 2022